

Extremely confined gap plasmon modes: when nonlocality matters

Sergejs Boroviks,^{1,2} Zhan-Hong Lin,² Vladimir A. Zenin,¹ Mario Ziegler,² Andrea Dellith,² P. A. D. Gonçalves,¹ Christian Wolff,¹ Sergey I. Bozhevolnyi,^{1,3} Jer-Shing Huang,^{2,4,5,6} and N. Asger Mortensen^{1,3}

¹Center for Nano Optics, University of Southern Denmark, Campusvej 55, DK-5230 Odense M, Denmark

²Leibniz Institute of Photonic Technology, Albert-Einstein Straße 9, 07745 Jena, Germany

³Danish Institute for Advanced Study, University of Southern Denmark, Campusvej 55, DK-5230 Odense M, Denmark

⁴Abbe Center of Photonics, Friedrich-Schiller-Universität Jena, 07743 Jena, Germany

⁵Research Center for Applied Sciences, Academia Sinica, 128 Sec. 2,

Academia Road, Nankang District, 11529 Taipei, Taiwan

⁶Department of Electrophysics, National Yang Ming Chiao Tung University, 1001 University Road, 30010 Hsinchu, Taiwan

(Dated: November 16, 2021)

Historically, the field of plasmonics has been relying on the framework of classical electrodynamics, with the local-response approximation of material response being applied even when dealing with nanoscale metallic structures. However, when approaching the atomic-scale confinement of the electromagnetic radiation, mesoscopic effects are anticipated to become observable, e.g., those associated with the nonlocal electrodynamic surface response of the electron gas. We investigate nonlocal effects in propagating gap surface plasmon modes in ultrathin metal–dielectric–metal planar waveguides, exploiting monocrystalline gold flakes separated by atomic-layer-deposited aluminum oxide. We use scanning near-field optical microscopy to directly access the near-field of such confined gap plasmon modes and measure their dispersion relation (via their complex-valued propagation constants). We compare our experimental findings with the predictions of the generalized nonlocal optical response theory to unveil signatures of nonlocal damping, which becomes appreciable for smaller dielectric gaps.

INTRODUCTION

One of the appealing features of plasmonics—the possibility to squeeze light beyond the diffraction limit and guide electromagnetic energy in waveguides with subwavelength dimensions [1–3]—has remained at the heart of the research community for several decades [4]. Such tight focusing is only possible due to unique properties of the surface-plasmon polariton (SPP), being a collective oscillation of the free charge-carriers in metals coupled with light fields [5]. Various configurations, designs, and materials for plasmonic systems have been studied from both fundamental and applied perspectives, attempting to realize a diversity of functional devices, ranging from plasmonic integrated circuitry [6] to metasurface-based flat optical components [7].

In particular, many devices are based on metal–dielectric–metal (MDM) heterostructures, which support gap surface plasmon (GSP) modes [8]. Gap surface plasmons can lead to substantial electric-field enhancements inside the dielectric gap, which can tremendously enhance linear and nonlinear optical processes [9], and may be exploited for various applications of plasmon-enhanced light–matter interactions, e.g., surface-enhanced Raman spectroscopy (SERS) [10] or Purcell enhancement of the emission rate of single-photon sources [11, 12]. Furthermore, MDM heterostructures may be engineered to achieve larger mode propagation lengths with better field confinements when compared with other SPP modes [13, 14]. The GSP modes supported by such waveguides were extensively studied by various experimental methods, including far-field techniques [15, 16] and scanning near-field optical microscopy (SNOM) [17, 18].

Many of the above-mentioned ambitions, along with the promise of realizing plasmonic waveguides for integration

(or even replacement) of conventional photonic waveguides, largely rely on the aspiration of significantly mitigating Ohmic losses in metals [19, 20]. Indeed, some progress in the development of traditional and alternative plasmonic materials has been made [21, 22]. Moreover, with advances in colloidal synthesis methods of traditional plasmonic materials it became possible to grow monocrystalline gold (Au) flakes with high aspect ratio—few tens of nanometers in thickness and up to several hundreds of square microns in surface area [23, 24]. Along with the improvement in nanofabrication techniques, such as focused ion beam (FIB) milling, this progress allowed the fabrication of plasmonic nanocircuitry [25, 26] and plasmonic nanoantennas [27, 28] with superior quality. Furthermore, monocrystalline Au flakes present as a “playground” material platform for experimental studies of fundamental aspects of plasmonics [29–36].

Many of the novel aspects in plasmonics have emerged and developed from considerations rooted in classical electrodynamics and the local-response approximation (LRA) for the interaction of light with the free-electrons in metals [5]. However, in recent years there has been increasing attention to quantum plasmonics [37–39] and the importance of quantum corrections to classical electrodynamics of plasmonic nanostructures [40–45], including nonlocal effects impacting GSP modes in MDM structures with ultranarrow gaps [46, 47]. This has contributed to a general consensus that in addition to bulk losses in plasmonic metals, there is an additional contribution in metallic surfaces associated with nonlocal effects [20, 41, 45].

The dominant microscopic mechanism contributing to nonlocal losses is Landau damping [48], which becomes especially pronounced at large plasmonic mode propagation vectors, i.e., manifesting also in MDM structures with very small dielectric gaps. While *ab initio* approaches in principle account for such

quantum nonlocal effects [49], quantum corrections to the LRA may also be explored semi-analytically using either hydrodynamic models or a surface-response formalism (SRF) [45]. In particular, the use of the Feibelman d -parameters [50] has in recent years been revived in the context of nanogap structures and related plasmonic phenomena [44, 51–56].

At the same time, there has been modest progress in experimental investigations of extremely confined propagating GSP modes as far as nonlocal corrections to the GSP dispersion in nanometer-sized gaps are concerned. The most relevant characterization of GSP modes is associated with observations of extreme splitting of symmetric and antisymmetric eigenmodes in side-by-side aligned single-crystalline Au nanorod dimers with atomically defined gaps reaching $\sim 5 \text{ \AA}$ [57]. While the experimentally measured resonance wavelengths could be accounted for without involving quantum nonlocal effects, experimentally measured resonance quality factors for GSP-based resonances were noted to be significantly lower than those predicted by the classical, local-response theory [57]. This qualitative observation tallies well with the analysis of the Landau damping influence on the GSP dispersion for nanometer-sized gaps that revealed practically no difference between local and nonlocal considerations of the real part of the GSP propagation constant, while showing progressively strong increase of the GSP propagation loss for the gaps below 10 nm [48]. Given the great importance of the GSP-based configurations for a wide range of plasmon-mediated light–matter interactions [9] and propagation losses determining the quality factors of the associated resonances, it is crucial to experimentally establish a benchmark for the nonlocal (i.e., Landau or surface collision) damping associated with extremely confined GSP modes.

In this work, we present an experimental study of extremely confined GSP modes in MDM structures fabricated out of monocrystalline Au flakes and atomic-layer-deposited (ALD) ultrathin aluminum oxide (Al_2O_3) films. The use of crystalline metal and high-quality dielectric material is crucial for reducing bulk and surface-roughness related losses to the minimum, thus opening a doorway to explore nonlocality [46]. The concept of the experiment is schematically illustrated in Fig. 1. Using a scattering-type SNOM (s-SNOM) [58], we obtain near-field (NF) maps of propagating GSP modes, which exhibit, to the best of our knowledge, a record-high experimentally demonstrated effective-mode index, reaching values of approximately 6.2 in the case of a ~ 2 nm-thick gap at $\lambda_0 = 1550$ nm excitation wavelength. Further analysis of the experimental data from a range of samples suggests signatures of gap-dependent nonclassical damping, being especially pronounced in samples with dielectric gap thicknesses less than 5 nm. We show that such observations are compatible with a nonlocal interpretation in terms of the so-called generalized nonlocal optical response (GNOR) theory [41], and provide an estimate of the diffusion constant that accounts for nonlocal damping. Incidentally, although the microscopic origin of the diffusion constant in GNOR represents carrier-scattering, it can also impersonate other sources of nonlocal damping (e.g., Landau damping) in a phenomenological fashion.

QUANTUM NONLOCAL CORRECTIONS TO THE GSP DISPERSION RELATION

The dispersion relation of the fundamental GSP mode in a MDM structure is generally given by [46]

$$\tanh\left(\frac{\kappa_d t_d}{2}\right) = -\frac{\kappa_m \varepsilon_d}{\kappa_d \varepsilon_m} (1 + \delta_{\text{nl}}), \quad (1a)$$

which reduces to the LRA expression of Economou [5] in the absence of nonlocal corrections (i.e., $\delta_{\text{nl}} \rightarrow 0$). Here, t_d is the thickness of the dielectric gap, whereas the out-of-plane components of the wavevectors are defined as

$$\kappa_j = \sqrt{q^2 - \varepsilon_j k_0^2} \quad \text{for } j \in \{d, m\}, \quad (1b)$$

where q is the GSP propagation constant, $k_0 \equiv \omega/c = 2\pi/\lambda_0$ is the free-space wavevector, and $\varepsilon_d \equiv \varepsilon_d(\omega)$ and $\varepsilon_m \equiv \varepsilon_m(\omega)$ are the relative permittivities (q -independent) of the dielectric and the metal, respectively.

Within the nonlocal hydrodynamic formalism [41, 42, 45], the nonlocal response introduces q -dependence in the material response (giving rise to the a nonlocal response in the corresponding real-space representation) [46]

$$\delta_{\text{nl}}(q, \omega) = \frac{q^2}{\kappa_{\text{nl}} \kappa_m} \frac{\varepsilon_m - \varepsilon_\infty}{\varepsilon_\infty}, \quad (2a)$$

$$\kappa_{\text{nl}} = \sqrt{q^2 - \frac{1}{\xi^2} \frac{\varepsilon_m}{\varepsilon_\infty}}. \quad (2b)$$

The nonlocal wavenumber $\kappa_{\text{nl}} \equiv \kappa_{\text{nl}}(q, \omega)$ enters in the hydrodynamic model of plasmonics as an additional longitudinal wave [42], with the nonlocal length scale ξ given by [42, 45].

$$\xi^2 = \frac{(3/5)v_F^2}{\omega(\omega + i\gamma)} + \frac{\mathcal{D}}{i\omega}. \quad (2c)$$

Here, the first term originates from the Thomas–Fermi theory of metals [42], with v_F being the Fermi velocity. The second term is an addition from GNOR model, with \mathcal{D} being the diffusion constant, and embodies the nonlocal damping. Finally, $\varepsilon_\infty \equiv \varepsilon_\infty(\omega)$ is a heuristic frequency-dependent parameter originating from the Drude LRA model [$\varepsilon_m \equiv \varepsilon_\infty - \omega_p^2/(\omega^2 + i\gamma\omega)$] that takes into account polarization due to the presence of positively charged atomic cores and interband transitions in the background of the quasi-free electron gas.

While the quantum-corrected dispersion relation (1a) originates from a hydrodynamic treatment of the nonlocal response of the metals (with $\text{Re}\{\delta_{\text{nl}}\} \propto v_F$ and $\text{Im}\{\delta_{\text{nl}}\} \propto \sqrt{\mathcal{D}}$) [42], we emphasize that in a SRF [45, 50], it can equally well be expressed in terms of the Feibelman parameter for the centroid of the induced charge [50], i.e., $\delta_{\text{nl}} \propto d_\perp$ (see Supplementary Section 7). For convenience, we will use the effective-mode index $n_{\text{GSP}} \equiv q/k_0 = \text{Re}\{n_{\text{GSP}}\} + i\text{Im}\{n_{\text{GSP}}\}$ and thus discuss all our results in terms of this dimensionless and complex-valued

quantity. Naturally, the larger $\text{Re}\{n_{\text{GSP}}\}$, the stronger is the confinement of electromagnetic field. In the spirit of the above treatment where $\delta_{nl} \ll 1$, nonlocality is expected to make only a small correction, which can nevertheless become sizable for large GSP wavevectors (that are promoted by small, nanometer-scale dielectric gap thicknesses, see schematic inset in Fig. 1), or, equivalently, for large values of $\text{Re}\{n_{\text{GSP}}\}$. Intuitively, $\text{Re}\{n_{\text{GSP}}\} \gg \text{Im}\{n_{\text{GSP}}\}$ is required for rendering quantum nonlocal effects experimentally observable. To enter this regime, the surface-response function $\text{Re}\{d_{\perp}\}$ should not be negligible in comparison to t_d , thus calling for nanofabrication techniques that can controllably realize MDM structures with sub-10-nanometer gaps. For sub-nanometric gaps with $t_d \lesssim |\text{Re}\{d_{\perp}\}|$, additional quantum mechanical effects (e.g., tunneling, electronic spill-out) may be needed to be accounted for [38, 52].

RESULTS

We experimentally study the dependence of the GSP spectral features on the thickness of the dielectric gap t_d ; to that end. We have fabricated five different planar MDM structures with varying t_d (nominally 2, 3, 5, 10, and 20 nm), along with tailored waveguide couplers. As previously mentioned, in order to explore potential signatures of nonlocal effects, it is essential to reduce as much as possible all losses of intrinsic origin (i.e., classical, bulk loss), but also those related to fabrication imperfections, such as surface roughness, contamination of metal and dielectric materials with impurities, etc. Therefore, we have utilized monocrystalline Au flakes as metal layers, whereas for the dielectric material in the core of the MDM structure we have employed plasma-assisted ALD of Al_2O_3 layers which allows controlled growth of homogeneous dielectric layers with approximately 2.2 Å precision (see Methods and Fig. S1 for details).

Figure 2 shows optical and scanning electron microscope (SEM) micrographs of a fabricated sample with a 3 nm dielectric gap, revealing too the FIB-milled tapered waveguide coupler. This element of the sample design and fabrication is of particular importance, since due to the large wavevector mismatch between free-space light and confined GSP modes, excitation of the latter with a Gaussian laser beam is not efficient. As such, it is necessary to provide a compact and adequate coupling mechanism, which is critical to obtain sufficiently strong signal in SNOM measurements. Due to the short GSP propagation length ($L_{\text{GSP}} \equiv [2 \text{Im} q]^{-1}$ is less than 0.5 μm for a 2 nm dielectric gap), a typical grating coupler schemes [59] becomes unsuitable. The periodicity of the grating Λ required by the phase-matching condition $q = k_0 + k_{\text{grating}} = k_0 \pm 2\pi m/\Lambda$ (with m being an integer number) even for a grating with just 3 periods, is comparable with the GSP propagation length. Therefore, in order to improve the coupling efficiency while maintaining a compact device, we exploited a tapered waveguide coupler design [60] and optimized its geometrical parameters for each dielectric gap thicknesses (see Methods and Supplementary

Section 6 for details).

Another important aspect of the design and fabrication of the MDM waveguides concerns the thickness of the upper Au layer, t_u . On the one hand, this upper layer needs to be sufficiently thin to make the NF of the ultraconfined GSP modes accessible to the s-SNOM tip, which scatters only weak evanescent tails of the mode penetrating through the top flake. On the other hand, t_u should be large enough to avoid significant modification of the GSP mode by undesired hybridization with the bare, single-interface SPP mode at the top air–Au interface. In both cases, the characteristic length-scale is the skin depth, making it a challenging task to fulfill both requirements. However, after thorough work on noise suppression in our SNOM, we managed to obtain near-field maps with sufficient signal-to-noise ratio for an upper-flake thickness of ~50 nm, for which the hybridization between the fundamental GSP and the single-interface SPP mode is negligible (see Fig. S6 in Supplementary Information). Furthermore, atomic flatness of the monocrystalline Au flakes allows to reduce the noise induced by surface roughness in near-field measurement, which is an important aspect for such low-signal measurements.

Using the capabilities of our s-SNOM setup to measure both amplitude and phase, as illustrated in Fig. 3(a) (detailed descriptions of the setup can be found in the Methods section), we have obtained complex NF maps showing the propagating GSP modes in all the fabricated samples. As an example, Figs. 3(b) and (c) show pseudo-color images of the electric NF amplitude $|E_{\text{NF}}|$ and its real part $\text{Re}\{E_{\text{NF}}\}$, respectively, for the sample with $t_d = 3$ nm (NF maps of all other samples are provided in Fig. S2). One-dimensional Fourier-transformation of the recorded NF maps along the GSP propagation direction ($x \rightarrow k_x$, as illustrated in Fig. 3(d) via the normalized absolute value of the transformed image) and averaging of the $E(k_x)$ spectrum along the y-axis direction, allows us to extract the real part of the GSP effective-mode index. As exhibited in Fig. 3(e), the NF spectrum has peaks at two spatial frequencies, which correspond to two distinct propagating modes. The first one, with an effective-index of approximately unity, can be attributed to free-space light at an oblique incidence or to SPP modes in the topmost air–Au interface. The other contribution corresponds to the GSP mode and manifests as a peak at an effective-index slightly exceeding $\text{Re} n_{\text{GSP}} \approx 5.1$. We note the absence of any significant contribution at a corresponding negative value ($\text{Re} n_{\text{GSP}} \approx -5.1$), which could indicate GSP back-scattering ($k_x \rightarrow -k_x$) due to surface roughness, potentially competing with nonlocal effects [61]. Moderate roughness-induced scattering may result in the broadening of the forward-scattering peak ($k_x \rightarrow k_x + \Delta k_x$, $\Delta k_x \ll k_x$), which would effectively manifest in a slightly increased imaginary part of the wavevector.

Further data post-processing, namely filtering of the NF maps with selecting only spatial frequencies in the vicinity of n_{GSP} in the Fourier domain, allows us to clean up interference with other near-fields as well as to reduce the noise, and retrieve the spatial evolution of the pure GSP mode along the propagation direction. Figure 4(a) illustrates the results of

that procedure, showing how the GSP wavelength is shortened ($\text{Re } n_{\text{GSP}}$ increased) and exhibits a faster decay (i.e. increasing $\text{Im } n_{\text{GSP}}$) as t_d is reduced from $t_d = 20$ nm down to 2 nm. The propagation length of the GSP modes can be estimated by fitting an exponential envelope to the $|E_{\text{NF}}|$ field. Further details about NF map processing can be found in Supplementary Section 2.

The parametric plot in Fig. 4(b) summarizes the experimental results (square data-points with error bars) and contrasts them against classical LRA calculations (dashed curve; open circles) as well as to those based on the GNOR model (solid curve; filled circles). In both calculations, we used experimentally obtained material parameters at $\lambda_0 = 1550$ nm from literature, namely, $\epsilon_m = -106.62 + 6.1257i$ for monocrystalline Au from Olmon *et al.* [62] and $\epsilon_d = 2.657$ for Al_2O_3 from Boidin *et al.* [63]. The Drude model parameters which enter the nonlocal correction factor δ_{nl} , were obtained by fitting the experimental data from Olmon *et al.* in the 1000–2000 nm wavelength range, yielding $\hbar\omega_p = 8.29$ eV, $\hbar\gamma = 47.72$ meV and $\epsilon_\infty = 2.61$; a tabulated value for gold’s Fermi velocity $v_F = 1.4 \times 10^6$ m s⁻¹ was used [64]. With this, a fit to our experimental data provides an estimate of the diffusion constant as $\mathcal{D} = 3.6 \times 10^{-3}$ m² s⁻¹. Even though the slope of the parametric curves is sensitive to the exact value of ϵ_m (see Fig. S3), we deliberately invoke data from Olmon *et al.* [62], being appropriate for descriptions of optical response of monocrystalline Au flakes [23].

As the LRA represents a minimal model for the light–matter interactions (invoking the most optimistic anticipations of materials’ losses), the gray-shaded area of this parametric regime in Fig. 4(b) would be “prohibited”. Within the measurement accuracy of our s-SNOM experiment, all the data points indeed fall outside this regime, except for points corresponding to the large gaps, where quantum nonlocal contributions become negligible and the solid line asymptotically approaches the LRA curve. However, for the smaller gaps the deviations of the experimental data from the LRA curve suggest evidence for including gap-dependent broadening mechanisms in theoretical treatments of the ultraconfined GSP modes, e.g., nonlocal surface-scattering corrections.

DISCUSSION

Nonlocal corrections to the classical, local-response electrodynamics have traditionally been extracted from optical measurements by confronting experimental data with classical predictions based on the LRA that invoke precise information about morphology obtained by other structural characterization means, e.g., SEM images revealing particle sizes, gap sizes, etc. (see, for instance, Refs. [65–71]). The success of these approaches to determine nonlocal corrections relies fully from the ability to correlate spectral shifts of resonances with accurate structural information on the morphology, which is no simple task even with state-of-the-art electron microscopy. Other approaches utilized well-controlled spacer materials, which

are challenging to work with, such as gaps formed by varying numbers of stacked graphene layers [72, 73], while graphene plasmons may also be used on their own to unveil nonlocal quantum effects in nearby metals and to probe surface-response functions [55].

As shown in Fig. 4, our analysis of GSP propagation partially eliminates the above-noted challenge since experimentally measured n_{GSP} data can be considered in a parametric way (where t_d is varied through different, but otherwise identical devices) and can be confronted by theory in the same way, i.e. by plotting solutions to Eq. (1a) for varying t_d . As shown in Fig. S5 of the Supplementary Information, the slope of the LRA dispersion curve in this parametric space is nearly independent of ϵ_d . This relaxes the need for detailed quantification of the possible deviations of ϵ_d and t_d (as fabricated) from its nominal values (as intended in the initial design). While we note that the real part of n_{GSP} obtained in experiments is consistently smaller than the predictions of both the LRA and calculations incorporating nonlocal corrections, this fact does not deny nor contradict our analysis in the parametric way, as explained above. Nevertheless, a possible explanation for this could be attributable to either presence of an air void or an additional dielectric layer between the Au flakes and the ALD film. The former could be present due to poor adhesion or other fabrication imperfection (for example, contamination with small particles that suspend the upper Au flakes slightly above the ALD layer), while the latter might appear as residuals of the organic molecules from the Au crystal growth solution.

The diffusion constant \mathcal{D} representing the carrier scattering was obtained from a fit to the experimental data, $\mathcal{D} \simeq 3.6 \times 10^{-3}$ m² s⁻¹, corresponding to a carrier-scattering length of the order $\sqrt{2\pi\mathcal{D}/\omega_p} \approx 1.34$ nm, which is just few fractions of nanometer smaller than the reported value of 1.9 nm [64]. We emphasize that we have refrained from any attempt to fit the real part of ξ , related to the Fermi velocity v_F , to force nonlocal predictions to fit even better the experimental data, as the value of 1.4×10^6 m s⁻¹ is well-established and was obtained independently in more dedicated and specific experiments. Instead, we would rather argue that our results offer a way to experimentally infer the value of d_\perp from experiment—admittedly being a determination of the surface-response function for this particular wavelength only and for this particular interface between single-crystalline Au and Al_2O_3 [i.e., $d_\perp^{\text{Al}_2\text{O}_3\text{-Au}}(\omega_0)$]. In principle, this procedure amounts to a fitting-extraction of the dimensionless quantity d_\perp/t_d , so that any inevitable uncertainties in t_d (actual deviations from nominal values) would in practice limit the accuracy by which we could in turn estimate d_\perp . Since theory accounts, including *ab initio* predictions, suggest that d_\perp is to be found in the ångström range [45, 56], we would need to experimentally determine t_d with atomic-scale accuracy, which remains a significant challenge as mentioned above. The fitting of the data with Eq. (1a) gives a value of $\delta_{\text{nl}} = -0.0075 + 0.07i \pm (0.0007 + 0.02i)$ for the smallest studied dielectric gap ($t_d = 2$ nm), which indeed meets our initial expectation that $|\delta_{\text{nl}}| \ll 1$. While we have here promoted a nonlocal interpretation for this observed gap-

dependent broadening, we emphasize that in principle this could also be qualitatively explained in the LRA by invoking other more lossy material-response models (see Fig. S5 in Supplementary Information) that seek to phenomenologically mimic additional effects of roughness, grain boundaries, etc. While our experiments cannot totally reject such alternative explanations, they would perhaps appear less obvious for our samples with a deliberate combined use of monocrystalline metals and ALD layers.

In summary, we have conducted an experimental study of record-high GSP mode-index in MDM structures comprised of a high-quality plasmonic material—monocrystalline Au flakes and ultrathin ALD-deposited Al_2O_3 films. By analyzing the s-SNOM signal from a samples with different t_d , we have found signatures of gap-dependent broadening, as captured by a generalized hydrodynamic model of plasmonics [41], which becomes progressively more significant for smaller dielectric gap thicknesses that give rise to higher effective-mode indices. Our results suggest that quantum nonlocal corrections, previously proposed theoretically, must be taken into account when treating extremely confined gap plasmon modes supported by MDM structures with sub-10-nanometer dielectric gaps.

METHODS

Sample fabrication

The fabrication recipe flowchart diagram can be found in Supplementary Information (see Fig. S1). Below we provide details about particular fabrication steps and used equipment.

Synthesis of monocrystalline Au flakes. Monocrystalline Au flake samples were prepared using a recipe adopted from reference [24]. In short, thin and flat Au crystals were synthesized on BK-7 glass substrates via endothermic reduction of chloroauric acid ($\text{HAuCl}_4 \cdot 3\text{H}_2\text{O}$) in ethylene glycol ($\text{C}_2\text{H}_6\text{O}_2$). All reagents were purchased from Sigma-Aldrich. The substrates were put into a vial with the solution and kept in an oven at 90°C for 24 h. Afterwards, samples were cleaned sequentially in acetone, isopropyl alcohol (IPA) and distilled water and dried with a nitrogen blow. Each substrate carried a large number of Au flakes with diverse sizes and shapes, and suitable samples were selected by visual inspection using white-light optical microscopy.

FIB milling of waveguide couplers. Milling of tapered waveguide coupler structures in monocrystalline Au flakes was performed using a gallium (Ga) ion FIB instrument (Helios NanoLab G3 UC, FEI company), with beam oriented perpendicularly to the sample plane an accelerating voltage of 30 kV and an ion current of 7.7 pA. In a preparatory step, chips carrying Au flake samples that were selected in the previous fabrication step were coated with a thin (≈ 6 nm) conductive carbon layer with a Leica Sputter Coater LEICA EM ACE600 in order to discharge the sample directly on the glass substrate, subsequently removed by mild plasma etching during the next fabrication step.

ALD of dielectric gap layer. After FIB patterning, the samples were coated with 2, 3, 5, 10, and 20 nm-thick layers of Al_2O_3 using Oxford Plasma Technology OPAL ALD system (Bristol, UK) equipped with an inductively coupled plasma source. To avoid degradations of the samples, the aluminum oxide layer was deposited at very low substrate temperatures (30°C). As precursors we used trimethylaluminum (TMA) and oxygen plasma with dose times of 30 ms and 5 s, respectively. Between each dose step, the reaction chamber was purged with inert argon and nitrogen for 5 s. The ALD process is defined by two half-cycles of self-terminating single surface reactions of each precursor, resulting in highly homogeneous and conformal Al_2O_3 coatings with nearly perfect thickness control [74]. The growth per cycle was 2.2 \AA [75]. Hence, the desired film thickness was adjusted by the number of applied ALD-cycles.

Transfer and assembly of Au flakes. Upper Au flakes were transferred from the substrates at which they have been synthesized using customized 2D material transfer system (HQ+ graphene). Polydimethylsiloxane (PDMS) stamps (WF X4 Gel-Film from Gel-Pak) were used as a carrier substrates. Transfer was performed at elevated temperature of 130°C to promote adhesion of the Au flake to the target substrate.

Numerical electrodynamics simulations

Numerical simulations and optimization of the electro-dynamics of the tapered coupler geometric parameters were performed using a commercially available finite-element method (FEM) solver (COMSOL Multiphysics 5.4, Wave Optics module). Since a planar waveguide is considered, the simulation was performed in 2D space (i.e. no spatial variation along y -axis, see Fig. S8). Experimentally measured values of material optical parameters at 1550 nm wavelength were used: $\epsilon_m = -106.62 + 6.1257i$ for monocrystalline Au from Olmon *et al.* [62]; $\epsilon_d = 2.657$ for Al_2O_3 from Boidin *et al.* [63]; and $\epsilon = 2.1$ for the BK-7 glass.

Simulations were performed in a wavelength domain at $\lambda_0 = 1550$ nm using a Gaussian beam source in a scattered field formulation. Value of 0.15 was used as a numerical aperture of the Gaussian beam to mimic the experimental excitation conditions in the s-SNOM setup. Geometrical parameters of the tapered waveguide coupler (w_t , w_a , w_1 and w_2) were optimized using the Levenberg–Marquardt algorithm (available from the COMSOL Optimization module), while layer thicknesses were kept fixed.

Near-field measurements

NF measurements were performed with the aid of s-SNOM [58], using the transmission module of a customized commercially available setup (Neaspec). Pseudo-heterodyne demodulation allows to simultaneously obtain information about amplitude and phase of the NF signal. Fig. 3(a) shows a schematic diagram of the setup: the laser beam from a CW

telecom laser (with wavelength $\lambda_0 = 1550$ nm) is split into two interferometric arms using a beam splitter (BS). In the reference arm, the signal is modulated using an oscillating mirror (OM) driven at the frequency $f \approx 300$ Hz. In the other arm, the laser beam is focused onto the waveguide coupler of the sample using a parabolic mirror (PM), with a focused beam of full-width-half-max (FWHM) spot size ~ 3 μm . An atomic-force microscope (AFM) tip (Arrow NCpt from NanoWorld) rasterscans the surface of the sample (which simultaneously allows to obtain topography of the sample) in a tapping mode (at the frequency $f_d \approx 250$ kHz and amplitude ~ 50 nm) and scatters the optical NF that is collected by another PM. Finally, reference and measurement arms are combined with a BS to allow interferometric detection and subsequent pseudo-heterodyne demodulation. In order to suppress background (bulk scattering from the tip and sample), the signal is demodulated at high harmonics of tip's oscillation frequency, mf_d , with $m = 3$ for presented results.

REFERENCES

-
- [1] W. L. Barnes, A. Dereux, and T. W. Ebbesen, *Nature* **424**, 824 (2003).
- [2] D. K. Gramotnev and S. I. Bozhevolnyi, *Nat. Photon.* **4**, 83 (2010).
- [3] D. K. Gramotnev and S. I. Bozhevolnyi, *Nat. Photon.* **8**, 14 (2014).
- [4] A. I. Fernández-Domínguez, F. J. García-Vidal, and L. Martín-Moreno, *Nat. Photon.* **11**, 8 (2017).
- [5] E. N. Economou, *Phys. Rev.* **182**, 539 (1969).
- [6] V. J. Sorger, R. F. Oulton, R.-M. Ma, and X. Zhang, *MRS Bulletin* **37**, 728 (2012).
- [7] F. Ding, A. Pors, and S. I. Bozhevolnyi, *Rep. Prog. Phys.* **81**, 026401 (2018).
- [8] C. L. C. Smith, N. Stenger, A. Kristensen, N. A. Mortensen, and S. I. Bozhevolnyi, *Nanoscale* **7**, 9355 (2015).
- [9] J. J. Baumberg, J. Aizpurua, M. H. Mikkelsen, and D. R. Smith, *Nat. Mater.* **18**, 668 (2019).
- [10] J. Langer *et al.*, *ACS Nano* **14**, 28 (2020).
- [11] S. I. Bozhevolnyi and J. B. Khurgin, *Nat. Photon.* **11**, 398 (2017).
- [12] A. I. Fernández-Domínguez, S. I. Bozhevolnyi, and N. A. Mortensen, *ACS Photonics* **5**, 3447 (2018).
- [13] J. A. Dionne, L. A. Sweatlock, H. A. Atwater, and A. Polman, *Phys. Rev. B* **73**, 035407 (2006).
- [14] S. I. Bozhevolnyi and J. Jung, *Opt. Express* **16**, 2676 (2008).
- [15] J. A. Dionne, H. J. Lezec, and H. A. Atwater, *Nano Lett.* **6**, 1928 (2006).
- [16] M. J. Preiner, K. T. Shimizu, J. S. White, and N. A. Melosh, *Appl. Phys. Lett.* **92**, 113109 (2008).
- [17] E. Verhagen, J. A. Dionne, L. K. Kuipers, H. A. Atwater, and A. Polman, *Nano Lett.* **8**, 2925 (2008).
- [18] R. Deshpande, V. A. Zenin, F. Ding, N. A. Mortensen, and S. I. Bozhevolnyi, *Nano Lett.* **18**, 6265 (2018).
- [19] J. B. Khurgin and G. Sun, *Appl. Phys. Lett.* **96**, 181102 (2010).
- [20] J. B. Khurgin, *Nat. Nanotechnol.* **10**, 2 (2015).
- [21] G. V. Naik, V. M. Shalaev, and A. Boltasseva, *Adv. Mater.* **25**, 3264 (2013).
- [22] K. M. McPeak, S. V. Jayanti, S. J. P. Kress, S. Meyer, S. Iotti, A. Rossinelli, and D. J. Norris, *ACS Photonics* **2**, 326 (2015).
- [23] B. Hoffmann, M. Y. Bashouti, T. Feichtner, M. Mačković, C. Dieker, A. M. Salaheldin, P. Richter, O. D. Gordan, D. R. T. Zahn, E. Spiecker, and S. Christiansen, *Nanoscale* **8**, 4529 (2016).
- [24] E. Krauss, R. Kullock, X. Wu, P. Geisler, N. Lundt, M. Kamp, and B. Hecht, *Cryst. Growth Des.* **18**, 1297 (2018).
- [25] J.-S. Huang, V. Callegari, P. Geisler, C. Bruening, J. Kern, J. C. Prangsma, X. Wu, T. Feichtner, J. Ziegler, P. Weinmann, M. Kamp, A. Forchel, P. Biagioni, U. Sennhauser, and B. Hecht, *Nat. Commun.* **1**, 150 (2010).
- [26] S. Kumar, T. Leißner, S. Boroviks, S. K. H. Andersen, J. Fiu-towski, H.-G. Rubahn, N. A. Mortensen, and S. I. Bozhevolnyi, *ACS Photonics* **7**, 2211 (2020).
- [27] R. Méjard, A. Verdy, O. Demichel, M. Petit, L. Markey, F. Herbst, R. Chassagnon, G. C. des Francs, B. Cluzel, and A. Bouhelier, *Opt. Mater. Express* **7**, 1157 (2017).
- [28] L. Kejík, M. Horák, T. Šíkola, and V. Křápek, *Opt. Express* **28**, 34960 (2020).
- [29] S. Viarbitskaya, A. Teulle, R. Marty, J. Sharma, C. Girard, A. Arbouet, and E. Dujardin, *Nat. Mater.* **12**, 426 (2013).
- [30] B. Frank, P. Kahl, D. Podbiel, G. Spektor, M. Orenstein, L. Fu, T. Weiss, M. Horn-von Hoegen, T. J. Davis, F.-J. Meyer zu Heringdorf, and H. Giessen, *Sci. Adv.* **3**, e1700721 (2017).
- [31] G. Spektor, D. Kilbane, A. K. Mahro, B. Frank, S. Ristok, L. Gal, P. Kahl, D. Podbiel, S. Mathias, H. Giessen, F. J. Meyer zu Heringdorf, M. Orenstein, and M. Aeschlimann, *Science* **355**, 1187 (2017).
- [32] S. Großmann, D. Friedrich, M. Karolak, R. Kullock, E. Krauss, M. Emmerling, G. Sangiovanni, and B. Hecht, *Phys. Rev. Lett.* **122**, 246802 (2019).
- [33] K. J. Kaltenecker, E. Krauss, L. Casses, M. Geisler, B. Hecht, N. A. Mortensen, P. U. Jepsen, and N. Stenger, *Nanophotonics* **9**, 509 (2020).
- [34] K. J. Kaltenecker, S. Rao D. S., M. Rasmussen, H. B. Lassen, E. J. R. Kelleher, E. Krauss, B. Hecht, N. A. Mortensen, L. Grüner-Nielsen, C. Markos, O. Bang, N. Stenger, and P. U. Jepsen, *APL Photonics* **6**, 066106 (2021).
- [35] S. Boroviks, T. Yezekyan, A. R. Echarri, F. J. García de Abajo, J. D. Cox, S. I. Bozhevolnyi, N. A. Mortensen, and C. Wolff, *Opt. Lett.* **46**, 833 (2021).
- [36] B. Munkhbat, A. Canales, B. Küçüköz, D. G. Baranov, and T. O. Shegai, *Nature* **597**, 214 (2021).
- [37] M. S. Tame, K. R. McEnery, Ş. K. Özdemir, J. Lee, S. A. Maier, and M. S. Kim, *Nat. Phys.* **9**, 329 (2013).
- [38] W. Zhu, R. Esteban, A. G. Borisov, J. J. Baumberg, P. Nordlander, H. J. Lezec, J. Aizpurua, and K. B. Crozier, *Nat. Commun.* **7**, 11495 (2016).
- [39] S. I. Bozhevolnyi and N. A. Mortensen, *Nanophotonics* **6**, 1185 (2017).
- [40] T. Christensen, W. Yan, S. Raza, A.-P. Jauho, N. A. Mortensen, and M. Wubs, *ACS Nano* **8**, 1745 (2014).
- [41] N. A. Mortensen, S. Raza, M. Wubs, T. Søndergaard, and S. I. Bozhevolnyi, *Nat. Commun.* **5**, 3809 (2014).
- [42] S. Raza, S. I. Bozhevolnyi, M. Wubs, and N. A. Mortensen, *J. Phys.: Cond. Matter* **27**, 183204 (2015).
- [43] P. A. D. Gonçalves, *Plasmonics and Light-Matter Interactions in Two-Dimensional Materials and in Metal Nanostructures: Classical and Quantum Considerations* (Springer Nature, 2020).
- [44] P. A. D. Gonçalves, T. Christensen, N. Rivera, A.-P. Jauho, N. A. Mortensen, and M. Soljačić, *Nat. Commun.* **11**, 366 (2020).

- [45] N. A. Mortensen, *Nanophotonics* **10**, 2563 (2021).
- [46] S. Raza, T. Christensen, M. Wubs, S. I. Bozhevolnyi, and N. A. Mortensen, *Phys. Rev. B* **88**, 115401 (2013).
- [47] V. Karanikolas, I. Thanopoulos, J. D. Cox, T. Kuroda, J.-i. Inoue, N. A. Mortensen, E. Paspalakis, and C. Tserkezis, *Phys. Rev. B* **104**, L201405 (2021).
- [48] J. B. Khurgin, *Faraday Disc.* **178**, 109 (2015).
- [49] A. Varas, P. García-González, J. Feist, F. J. García-Vidal, and A. Rubio, *Nanophotonics* **5**, 409 (2016).
- [50] P. J. Feibelman, *Prog. Surf. Sci.* **12**, 287 (1982).
- [51] T. V. Teperik, P. Nordlander, J. Aizpurua, and A. G. Borisov, *Phys. Rev. Lett.* **110**, 263901 (2013).
- [52] W. Yan, M. Wubs, and N. A. Mortensen, *Phys. Rev. Lett.* **115**, 137403 (2015).
- [53] T. Christensen, W. Yan, A.-P. Jauho, M. Soljačić, and N. A. Mortensen, *Phys. Rev. Lett.* **118**, 157402 (2017).
- [54] Y. Yang, D. Zhu, W. Yan, A. Agarwal, M. Zheng, J. D. Joannopoulos, P. Lalanne, T. Christensen, K. K. Berggren, and M. Soljačić, *Nature* **576**, 248 (2019).
- [55] P. A. D. Gonçalves, T. Christensen, N. M. R. Peres, A.-P. Jauho, I. Epstein, F. H. L. Koppens, M. Soljačić, and N. A. Mortensen, *Nat. Commun.* **12**, 3271 (2021).
- [56] A. R. Echarri, P. A. D. Gonçalves, C. Tserkezis, F. J. García de Abajo, N. A. Mortensen, and J. D. Cox, *Optica* **8**, 710 (2021).
- [57] J. Kern, S. Großmann, N. V. Tarakina, T. Häckel, M. Emmerling, M. Kamp, J.-S. Huang, P. Biagioni, J. C. Prangsma, and B. Hecht, *Nano Lett.* **12**, 5504 (2012).
- [58] F. Keilmann and R. Hillenbrand, *Philos. Trans. A* **362**, 787 (2004).
- [59] S. A. Maier, *Plasmonics: Fundamentals and Applications* (Springer-Verlag, 2007).
- [60] D. F. P. Pile and D. K. Gramotnev, *Appl. Phys. Lett.* **89**, 041111 (2006).
- [61] G. Hajisalem, Q. Min, R. Gelfand, and R. Gordon, *Opt. Express* **22**, 9604 (2014).
- [62] R. L. Olmon, B. Slovick, T. W. Johnson, D. Shelton, S.-H. Oh, G. D. Boreman, and M. B. Raschke, *Phys. Rev. B* **86**, 235147 (2012).
- [63] R. Boidin, T. Halenkovič, V. Nazabal, L. Beneš, and P. Němec, *Ceram. Int.* **42**, 1177 (2016).
- [64] N. D. Ashcroft and N. D. Mermin, *Solid State Physics* (Saunders College Publishing, 1976).
- [65] H. T. Miyazaki and Y. Kurokawa, *Phys. Rev. Lett.* **96**, 097401 (2006).
- [66] H. Duan, A. I. Fernández-Domínguez, M. Bosman, S. A. Maier, and J. K. W. Yang, *Nano Lett.* **12**, 1683 (2012).
- [67] C. Ciraci, R. Hill, J. Mock, Y. Urzhumov, A. Fernández-Domínguez, S. Maier, J. Pendry, A. Chilkoti, and D. Smith, *Science* **337**, 1072 (2012).
- [68] J. A. Scholl, A. L. Koh, and J. A. Dionne, *Nature* **483**, 421 (2012).
- [69] S. Raza, N. Stenger, S. Kadkhodazadeh, S. V. Fischer, N. Kostešha, A.-P. Jauho, A. Burrows, M. Wubs, and N. A. Mortensen, *Nanophotonics* **2**, 131 (2013).
- [70] S. Raza, S. Kadkhodazadeh, T. Christensen, M. Di Vecce, M. Wubs, N. A. Mortensen, and N. Stenger, *Nat. Commun.* **6**, 8788 (2015).
- [71] H. Shen, L. Chen, L. Ferrari, M.-H. Lin, N. A. Mortensen, S. Gwo, and Z. Liu, *Nano Lett.* **17**, 2234 (2017).
- [72] J. Mertens, A. L. Eiden, D. O. Sigle, F. Huang, A. Lombardo, Z. Sun, R. S. Sundaram, A. Colli, C. Tserkezis, J. Aizpurua, S. Milana, A. C. Ferrari, and J. J. Baumberg, *Nano Lett.* **13**, 5033 (2013).
- [73] D. A. Iranzo, S. Nanot, E. J. C. Dias, I. Epstein, C. Peng, D. K. Efetov, M. B. Lundberg, R. Parret, J. Osmond, J.-Y. Hong, J. Kong, D. R. Englund, N. M. R. Peres, and F. H. L. Koppens, *Science* **360**, 291 (2018).
- [74] B. Jang, J. Gargiulo, M. Ziegler, R. F. Ando, U. Hübner, S. A. Maier, and M. A. Schmidt, *Opt. Lett.* **45**, 196 (2020).
- [75] S. Yüksel, M. Ziegler, S. Goerke, U. Hübner, K. Pollok, F. Langenhorst, K. Weber, D. Cialla-May, and J. Popp, *J. Phys. Chem. C* **119**, 13791 (2015).

ACKNOWLEDGMENTS

We are grateful to S. Raza and T. Christensen for their early theory contributions [46] that motivated this experimental study. C.W. acknowledges funding from a MULTIPLY fellowship under the Marie Skłodowska-Curie COFUND Action (grant agreement No. 713694). S. I. B. acknowledges the support from VILLUM FONDEN (Villum Kann Rasmussen Award in Technical and Natural Sciences 2019). J.-S. H. acknowledges the support from Leibniz-IPHT (2020 Innovation Project) and DFG (HU 2626/3-1). N. A. M. is a VILLUM Investigator supported by VILLUM FONDEN (Grant No. 16498).

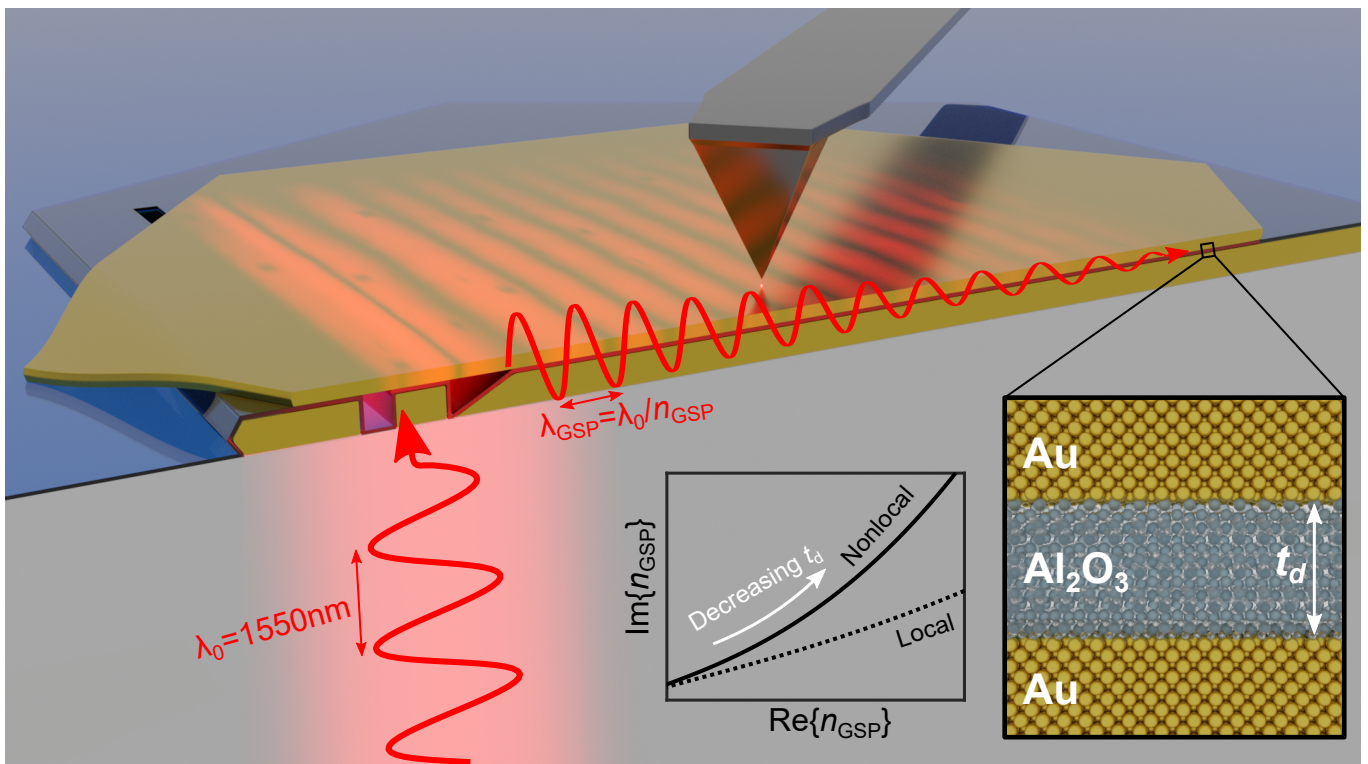


FIG. 1. Schematics of the experiment setup. The red curves schematically illustrate the electric-field profile of the excitation light (bottom left) and of the propagating GSP mode (in the sample) with group-index n_{GSP} . Insets show the parametric plot (varying the gap-size, t_d) of the GSP dispersion trends with and without nonlocal corrections, while at the bottom right it is shown a close-up of the MDM waveguide comprised of the single-crystalline gold (Au) flakes separated by a thin dielectric gap formed by atomic-layer deposition of aluminum oxide (Al_2O_3).

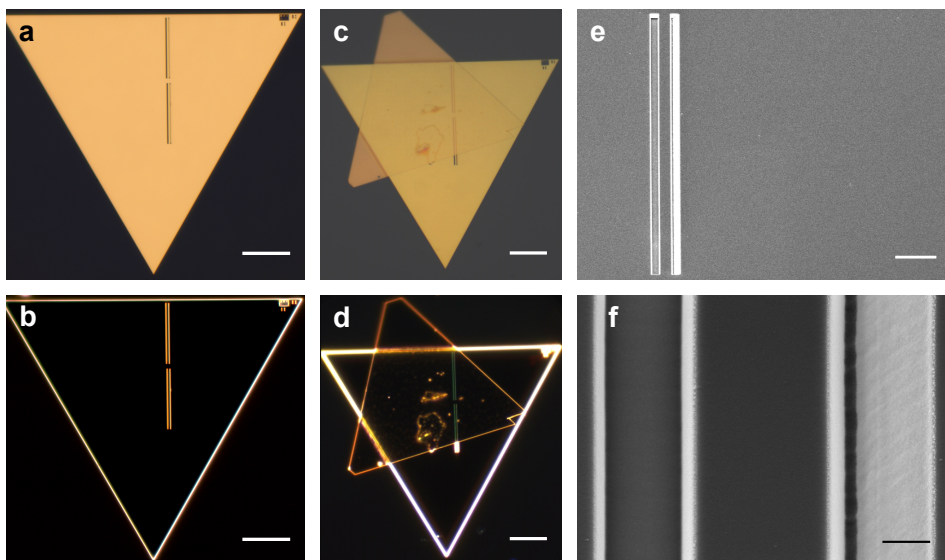


FIG. 2. **a** Bright- and **b** Dark-field optical images of the sample with a 3 nm Al_2O_3 layer before the transfer of the top flake. **c** Bright- and **d** Dark-field optical images of the sample after the transfer of the top flake. **e** SEM image of the flake during intermediate fabrication step and **f** close-up image of the FIB milled coupling element. Scale bars in panels **a–d** correspond to 10 μm , in panel **e** to 2 μm and in panel **f** to 50 nm.

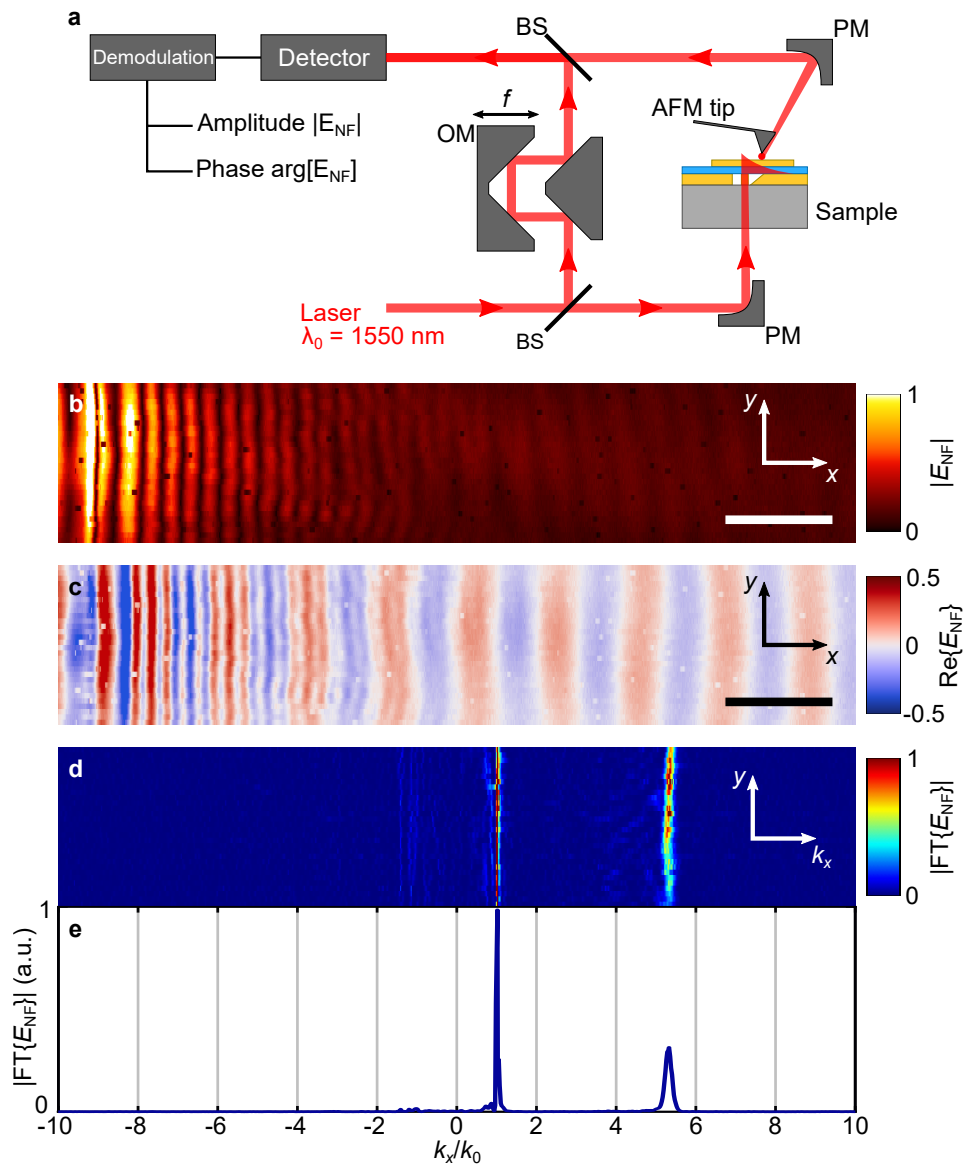


FIG. 3. **a** Schematic illustration of the s-SNOM setup (see Methods for details). Pseudo-color images of **b** amplitude and **c** real-part of the detected NF signal for the sample with 3 nm dielectric gap at $\lambda_0 = 1550$ nm excitation wavelength (scale bars: $2 \mu\text{m}$). **d** Amplitude of the Fourier transformation of the measured NF along the propagation coordinate ($x \rightarrow k_x$) and **e** its profile (averaged along the y -axis).

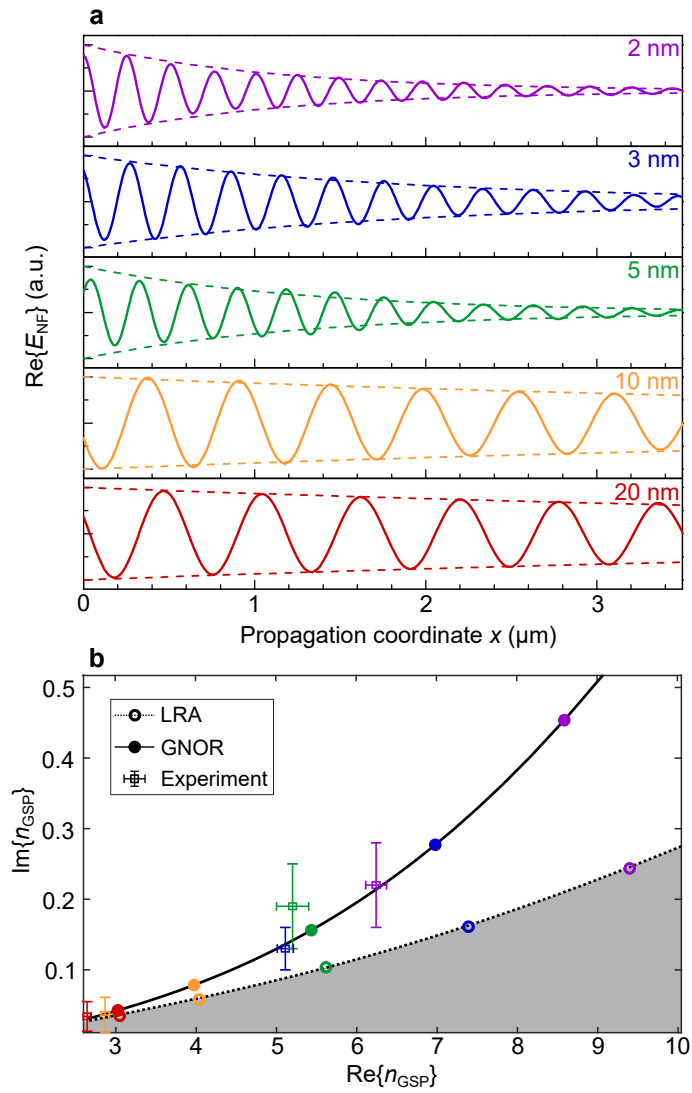


FIG. 4. **a** Real part (solid curves) and exponential envelopes (dashed curves) of the GSP mode profiles extracted from s-SNOM measurements for all five samples with indicated gap thickness. **b** Parametric plot of the effective-mode index n_{GSP} (excited at $\lambda_0 = 1550$ nm) for varying dielectric gap thickness: calculated using LRA (dashed curve; open circles), GNOR model (solid curve; filled circles) and experimentally obtained data (squares with error bars). Colors of the indicated points on the curves and experimental data points correspond to 2, 3, 5, 10 and 20 nm gap thicknesses, as in panel **a**.